Stability of charge-density waves under continuous variation of band filling in LaTe$_{2-x}$Sb$_x$ ($0 \leq x \leq 1$)

E. DiMasi[*]

Harrison M. Randall Laboratory of Physics, University of Michigan, Ann Arbor, Michigan 48109-1120

B. Foran

Willard H. Dow Laboratory of Chemistry, University of Michigan, Ann Arbor, Michigan 48109-1055

M. C. Aronson[†]

Harrison M. Randall Laboratory of Physics, University of Michigan, Ann Arbor, Michigan 48109-1120

S. Lee

Willard H. Dow Laboratory of Chemistry, University of Michigan, Ann Arbor, Michigan 48109-1055

We report the presence of charge-density waves (CDW's) in the planar square lattices of the layered compounds LaTe$_{2-x}$Sb$_x$ for $0 \leq x \leq 1$, which we have studied through electron microprobe analysis, powder- and single-crystal x-ray diffraction, and transmission electron microscopy. We have identified superlattice reflections with wave vectors spanning large parallel sheets of Fermi surfaces derived from extended-Hückel tight-binding band calculations performed on two-dimensional Te square sheets. As Sb substitutes for Te in LaTe$_2$, the band filling of the square sheets is continuously decreased, with essentially no deviation from the LaTe$_2$ substructure. Through the series, the CDW wave vector follows the changes in the Fermi surface. The CDW's are observed at room temperature and we see no evidence of significant disorder effects with Sb doping. This work establishes LaTe$_{2-x}$Sb$_x$ as a family of materials in which the CDW is dependent on Fermi-surface energetics, in contrast to other CDW materials in which lattice strain forces the structural distortion to remain commensurate. [S0163-1829(96)00140-3]

I. INTRODUCTION

The study of charge-density waves (CDW's) is important, because a successful description of the coupled electronic-lattice instability reflects on the broader issue of the electronic aspects of structural stability. In a CDW system, a structural distortion is stabilized by the formation of a gap which lowers the energy of electronic states below the Fermi level. This gap is a consequence of the periodicity of the distortion, and so the CDW optimally occurs at a wave vector which nests large parts of the Fermi surface. This picture successfully describes many systems in which the strain energy of the distortion is finely balanced against the energy gained by the imposition of the CDW gap, so that the instability is characterized by a small energy scale, with a structural transition often occurring below room temperature.[1–4] As the energetic difference between two structures becomes larger, there is less temptation to invoke the framework of a CDW instability, or to parametrize one structure as a distorted version of another. Ultimately the question of structural stability becomes one of arriving at the lowest-energy structure, in which states far from the Fermi level may contribute to the band energy of the system. To the extent that the states near the Fermi level do not play such a critical role in the stability of the distortion, the constraint relating the geometry of the undistorted Fermi surface to the periodicity of the distorted state is relaxed. As the Fermi surface becomes less important, the larger energy scales governing the structural instability may be more appropriately thought of in

terms of the bonding energy, or equivalently the lattice strain. A pertinent question is whether this extreme is qualitatively different from a CDW, or just an extension of the same mechanism to larger energy scales.

For illustration, some comparison of the relative importance of the Fermi-surface nesting criterion can be made across CDW families. BaBiO$_3$ has a distorted cubic structure comprised of Bi-O octahedra, in which alternating Bi atoms have inequivalent valences.[5] The charge density modulation leads to the expansion and contraction of corresponding Bi-O bond lengths, and the adoption of a supercell containing two formula units relative to the cubic substructure.[6] Electronic structure calculations indicate that the Fermi surface of the sublattice has perfect nesting for the half-filled band, and the usual interpretation of BaBiO$_3$ is that a very strong electron-phonon coupling drives the commensurate CDW.[7] The band filling in BaBiO$_3$ can be decreased by doping, for example, with Pb on the Bi site, or with K replacing Ba atoms.[8,9] Experimental studies of Ba$_{1-x}$K$_x$BiO$_3$ and BaBi$_{1-x}$Pb$_x$O$_3$ show that while the CDW gap is suppressed with increasing x, the distortion wave vector remains fixed until the CDW is completely destabilized at $x=0.65$ or 0.35 for Pb or K doping respectively.[8,10] In BaBiO$_3$, the doping studies show that the large energy scale of a breathing mode distortion causes the CDW wave vector to remain commensurate even as the Fermi-surface nesting vector is changed.[11]

Sharply contrasting behavior can be found among the transition-metal dichalcogenides MX_2. In these layered compounds the quasi-two-dimensional electronic structure drives

<u>54</u> 13 587

small amplitude Fermi-surface nesting CDW's,[12] while phonon modes with anomalies near the CDW wave vector are found to soften considerably near the CDW transition temperature,[13] reducing the strain energy of the distortion. In the MX_2, where the Fermi surface lies in the metal d bands, changes in the electron concentration can cause a corresponding change in the CDW wave vector. This has been demonstrated by the substitution of Ti for Ta in $1T\text{-}TaS_2$, which removes electrons from the d band, reducing the optimal Fermi-surface nesting vector. In $1T\text{-}Ta_{1-x}Ti_xS_2$ for $x \leq 0.9$, superlattice reflections were observed at wave vectors which followed the reduction in the Fermi-surface nesting vector, while the CDW is completely suppressed for TiS_2, where the bottom of the nesting band has been reached.[12] The band filling study in the case of the MX_2 indicates that here the energetics of the Fermi surface are the primary factors for CDW stability, in contrast to the $BaBiO_3$ family. However, two factors make it difficult to determine the role of the soft phonon in the MX_2. Cation disorder in metal doped MX_2 compounds substantially reduces the CDW transition temperatures, even for the case of isoelectronic dopants where Fermi-surface nesting is unchanged.[12] In these materials, deviation from the most favorable phonon wave vector, reduction of the number of nestable states at the Fermi surface, and disorder may contribute together to the decreased CDW transition temperatures in Ti-rich $1T\text{-}Ta_{1-x}Ti_xS_2$. In addition, the transition metal d character produces narrow bands, in which small changes in electron concentration yield large changes in the geometry of the calculated Fermi surface.[14] Since small doping steps are required to vary the band filling continuously, such a study is particularly vulnerable to the effects of compositional inhomogeneity in the MX_2.

The investigation of Fermi surface driven CDW's under the variation of band filling requires a system in which nesting vectors can be continuously tuned without introducing appreciable disorder. Recently, we have studied the layered rare-earth polychalcogenides RX_n in this context (R denotes rare earth; X denotes S, Se, or Te; $n=2, 2.5, 3$). The RX_n are comprised of chalcogen square lattices alternating with puckered rare-earth-chalcogen layers,[15–17] and previous studies of the RX_n demonstrated the presence of CDW's in the planar square sheets.[18–20] The distortions occur at wave vectors near those spanning large parallel sheets of Fermi surfaces calculated from two-dimensional square Se or Te lattices.[19,20] Band filling in the square sheets is controlled by charge transfer from the rare earths, leading to different nesting vectors for the stoichiometries RX_2 and RX_3. In the RTe_3, in-

commensurate CDW's have been observed, implying a strong role for Fermi-surface nesting.[20] The RSe_2 compounds host commensurate CDW's,[18] and because they occur at a plausible nesting vector, it is impossible to assess the relative importance of Fermi-surface nesting and lattice strain without experimental variation of the band filling.

In this paper we will show that the hole doped system $LaTe_{2-x}Sb_x$ is ideal for such a study. The Te s and p states produce bands with widths of ≈ 20 eV,[21] four times broader than the MX_2 bands (≈ 5 eV),[12] while the Fermi-surface geometry changes smoothly over a large range of band filling.[20] Since Sb has the same atomic core as Te but has one fewer valence electron, the substitution removes electrons from the square-sheet bands. Previous workers have reported that $LaTe_{2-x}Sb_x$ can be obtained as a solid solution for the range $0 \leq x \leq 1.5$, with Sb substituting for Te within the $LaTe_2$-type structure.[22,23] Using an alkali halide flux method, we have synthesized single crystals of $LaTe_{2-x}Sb_x$ with $0 \leq x \leq 1$. Through x-ray and electron diffraction we have identified CDW's at wave vectors which span the calculated Fermi surface over a large range of band filling. We find no evidence for disorder. Our results demonstrate the predominant role of Fermi-surface nesting for CDW's in square Te lattices.

II. EXPERIMENTAL DETAILS

Weighed amounts of La, Te, and Sb were sealed in evacuated quartz tubes with RbCl and LiCl salts and heated at 495 °C for 1–3 days, then kept at 700 °C for 5–7 days.[24] Products in the form of shiny blue-gray or purple platelets were examined by electron microprobe analysis.[25] Powder x-ray-diffraction data were recorded on an Enraf-Nonius Guinier camera.[26] Lattice constants were fit by least squares, and powder data were indexed, with the aid of the program LAZY-PULVERIX.[27] Single crystals were selected and mounted in sealed glass capillaries. Weissenberg and Precession photographs were recorded to search for superlattice diffraction. Single-crystal data were corrected for absorption semiempirically by ψ scans.[28] Data processing, structure solution, and refinement were facilitated by Siemens' software package SHELXTL.[29] For transmission electron microscopy (TEM), crystals were coarsely ground with a mortar and pestle and mounted on amorphous carbon film on copper grids. Selected area diffraction patterns were obtained using a JEOL 2000FX transmission electron microscope with a liquid-nitrogen cold stage, operating at 200 kV. Simulated diffraction patterns were calculated with the CERIUS^2 program.[30]

TABLE I. Nominal stoichiometries and results of electron microprobe analysis for $LaTe_{2-x}Sb_x$ compounds.

Nominal composition	Te:La atomic ratio	Sb:La atomic ratio	Measured stoichiometry
$LaTe_2$	2.00 ± 0.04		$LaTe_{2.0}$
$LaTe_{1.6}Sb_{0.4}$	1.76 ± 0.13	0.184 ± 0.005	$LaTe_{1.8}Sb_{0.2}$
$LaTe_{1.5}Sb_{0.5}$	1.64 ± 0.03	0.312 ± 0.006	$LaTe_{1.6}Sb_{0.3}$
$LaTe_{1.2}Sb_{0.8}$	1.38 ± 0.02	0.548 ± 0.011	$LaTe_{1.4}Sb_{0.5}$
$LaTe_{1.1}Sb_{0.9}$	1.19 ± 0.02	0.670 ± 0.027	$LaTe_{1.2}Sb_{0.7}$
$LaTe_{0.9}Sb_{1.1}$	0.98 ± 0.02	0.96 ± 0.04	LaTeSb (batch 1)
$LaTe_{0.8}Sb_{1.2}$	0.98 ± 0.02	0.97 ± 0.03	LaTeSb (batch 2)

TABLE II. Crystallographic data for $LaTe_{2-x}Sb_x$.

Empirical formula	$LaTe_{1.76}Sb_{0.18}$	$LaTe_{1.64}Sb_{0.31}$	$LaTe_{1.19}Sb_{0.67}$	$LaTeSb$
Formula weight	392.94	379.6	377.26	388.26
Crystal system	Orthorhombic	Orthorhombic	Orthorhombic	Orthorhombic
Space group	$Pmmn$ (59)	$Pmmn$ (59)	$Pmmn$ (59)	$Pmcn$ (62)[a]
Lattice (Å)	$a=4.4946$ (5)	$a=4.4495$ (6)	$a=4.4164$ (4)	$a=4.3776$ (5)
	$b=4.5371$ (7)	$b=4.5501$ (6)	$b=4.4486$ (5)	$a=4.4031$ (6)
	$c=9.2578$ (11)	$c=9.3165$ (14)	$c=9.4837$ (8)	$c=19.242$ (2)
Volume Z	188.79 (4) $Å^3$, 2	188.62 (5) $Å^3$, 2	188.32 (3) $Å^3$, 2	370.89 (7) $Å^3$, 4
Density (calculated)	6.912 Mg/m^3	6.673 Mg/m^3	6.724 Mg/m^3	6.953 Mg/m^3
Absorption coeff.	26.074 mm^{-1}	25.223 mm^{-1}	25.360 mm^{-1}	26.078 mm^{-1}
$F(000)$	322	311	310	640
Crystal size (mm)	$0.16\times0.16\times0.05$	$0.10\times0.10\times0.01$	$0.11\times0.20\times0.04$	$0.125\times0.15\times0.025$
θ range collected	4.40–29.97 deg.	4.38–29.96 deg.	4.30–34.99 deg.	4.24–29.99 deg.
Limiting indices	$-6\leqslant h\leqslant6$, $-6\leqslant k\leqslant6$,	$-6\leqslant h\leqslant6$, $-6\leqslant k\leqslant6$,	$-7\leqslant h\leqslant7$, $-7\leqslant k\leqslant7$,	$-6\leqslant h\leqslant6$, $-6\leqslant k\leqslant6$,
	$-13\leqslant l\leqslant13$	$-13\leqslant l\leqslant13$	$-15\leqslant l\leqslant15$	$-27\leqslant l\leqslant27$
Reflections collected	2030	2042	3102	3744
Independent reflections	336 [$R_{int}=0.0375$]	329 [$R_{int}=0.0396$]	492 [$R_{int}=0.1800$]	598 [$R_{int}=0.0501$]
Max. and min. trans.[b]	0.5442 and 0.1147	0.7604 and 0.2073	0.7702 and 0.4344	0.8818 and 0.2714
Data/restr./par's[c]	336/0/14	329/0/13	492/0/14	598/0/20
GooF$=S$ (on F^2)[d]	1.209	1.224	1.222	1.017
Final R [$I>2\sigma(I)$]	$R_1=0.0672$,[e]	$R_1=0.0420$,	$R_1=0.0612$,	$R_1=0.0346$,
	$wR_2=0.1742$,[f]	$wR_2=0.1127$,	$wR_2=0.1706$,	$wR_2=0.0885$,
R indices (all data)	$R_1=0.0686$,	$R_1=0.0451$,	$R_1=0.0613$,	$R_1=0.0421$,
	$wR_2=0.1753$,	$wR_2=0.1141$,	$wR_2=0.1707$,	$wR_2=0.0908$,
Extinction coefficient	0.014 (5)	0.012 (3)	0.052 (8)	0.0011 (3)
Diff. max./min. e $Å^3$	5.854/-7.208	5.741/-4.326	2.816/-8.165	2.673/-2.934

[a]The conventional setting for this space group is $Pnma$, with $a=19.242(2)$, $b=4.3776(5)$, $c=4.4031(6)$.
[b]Absorption corrections were calculated semiempirically from ψ scans for each crystal.
[c]Structures were solved by direct methods, and refined by full-matrix least squares on F^2 (SHELX-93).
[d]GooF$=S=\{\Sigma[w(F_o^2-F_c^2)^2]/(n-p)\}^{1/2}$: n is the number of reflections, p is the total number of parameters used, and weight$=w=1/[\sigma^2(F_o^2)+(0.0452P)^2+3.26P]$, where $P=[Max(F_o^2,0)+2F_c^2]/3$.
[e]$R_1=\Sigma||F_o|-|F_c||/\Sigma|F_o|$.
[f]$wR=\{\Sigma[w(F_o^2-F_c^2)^2]/\Sigma[w(F_o^2)^2]\}^{1/2}$.

The EHMACC software[31] was used for band-structure calculations.

III. EXPERIMENTAL RESULTS

A. Electron microprobe analysis

The samples were examined by electron microprobe analysis to determine their stoichiometry. Several crystals from each tube were examined, with 3–15 measurements taken on each crystal. Measurements on the $LaPO_4$, Te, and Sb standards varied with standard deviations of 1.4, 0.9, and 0.9 at. % respectively, which we take as a measure of the random instrumental error. For most $LaTe_{2-x}Sb_x$ batches, variation in the measured stoichiometries at different locations on a single platelet was found to be the same as that from crystal to crystal for each tube, and comparable to the

TABLE III. Powder and single-crystal x-ray structural characterizations of orthorhombic subcells of $LaTe_{2-x}Sb_x$ phases.

	Powder data			Single-crystal data		
Compound	a (Å)	b (Å)	c (Å)	a (Å)	b (Å)	c (Å)
$LaTe_2$	4.523 (1)	4.554 (1)	9.221 (3)			
$LaTe_{1.8}Sb_{0.2}$	4.490 (2)	4.539 (2)	9.257 (4)	4.4946 (5)	4.5371 (7)	9.2578 (11)
$LaTe_{1.6}Sb_{0.3}$	4.445 (1)	4.550 (1)	9.312 (1)	4.4495 (6)	4.5501 (6)	9.3165 (14)
$LaTe_{1.4}Sb_{0.5}$	4.4258 (4)	4.4836 (4)	9.4175 (8)			
$LaTe_{1.2}Sb_{0.7}$	4.417 (2)	4.454 (1)	9.474 (4)	4.4164 (4)	4.4486 (5)	9.4837 (8)
$LaTeSb$ (batch 1)	4.3739 (6)	4.4016 (5)	9.607 (2)			
$LaTeSb$ (batch 2)	4.374 (2)	4.401 (2)	9.616 (3)	4.4031 (6)[a]	4.3776 (5)[a]	9.621 (1)[a]

[a]Structure was refined in the supercell with $a_{super}=a_{sub}$, $b_{super}=b_{sub}$, $c_{super}=2c_{sub}$.

TABLE IV. Atomic coordinates ($\times 10^4$) and displacement parameters[a] ($\text{Å}^2 \times 10^3$) for $LaTe_{1.8}Sb_{0.2}$.

	x	y	z	U_{11}	U_{22}	U_{33}	U (eq)
La (1)	2500	2500	7258 (1)	8 (1)	12 (1)	8 (1)	9 (1)
Te (1)	2500	2500	3677 (1)	7 (1)	11 (1)	7 (1)	8 (1)
Sb/Te (2)	2500	−2500	−5 (2)	20 (1)	29 (1)	5 (1)	18 (1)

[a]The anisotropic displacement factor exponent takes the form $-2\pi^2[h^2a^{*2}U_{11}+\cdots+2hka^*b^*U_{12}]$. For $Pmmn$ $U_{23}=U_{13}=U_{12}=0$. U (eq) is defined as one-third of the trace of the orthogonalized U_{ij} tensor.

total error obtained on the calibration standards, about 3 at. %. This indicates that the samples within these tubes have uniform stoichiometry within the limits of our microprobe study. Larger variations of about 10 at. % were found for $LaTe_{1.8}Sb_{0.2}$, but since very few microprobe measurements could be made due to the small size of the crystals, we regard this result as questionable. Other compositions obtained were $LaTe_2$, $LaTe_{1.6}Sb_{0.3}$, $LaTe_{1.4}Sb_{0.5}$, $LaTe_{1.2}Sb_{0.7}$, and $LaTeSb$. We found that the amount of Sb incorporated into the samples was always less than that of the nominal composition of the starting materials. For $LaTe_{1.6}Sb_{0.3}$, $LaTe_{1.4}Sb_{0.5}$, and $LaTe_{1.2}Sb_{0.7}$, the measured Te and Sb atomic fractions do not add to yield a La:anion ratio of exactly 1:2. However, no Te or Sb deficiency could be confirmed by single-crystal x-ray refinements, and we surmise that the apparent off stoichiometry is due to systematic error in the microprobe calibration. Results of the microprobe analysis are summarized in Table I. Since the experimental error of the microprobe is much smaller than the difference between measured and nominal stoichiometries, we believe that the microprobe measurements provide the most reliable determination of the Sb content. We will refer to each compound by its measured stoichiometry, but we will model all compounds as fully occupied square sheets, as the small anion deficiency would make no appreciable difference in the band filling.

B. X-ray diffraction

Our x-ray-diffraction results for the $LaTe_{2-x}Sb_x$ substructure are essentially in agreement with earlier reports,[22] with minor differences. Guinier powder patterns of all $LaTe_{2-x}Sb_x$ phases with $0 \leq x \leq 1$ could be indexed in the $LaTe_2$ structure type, as reported previously.[22] The powder patterns of the reacted tube contents showed that our reactions produced mostly homogeneous samples, although in the batch producing $LaTe_{1.4}Sb_{0.5}$, weak lines were detected at low 2θ corresponding to minor amounts of $LaSb_2$. Single-crystal x-ray data were collected for $LaTe_{1.8}Sb_{0.2}$, $LaTe_{1.6}Sb_{0.3}$, $LaTe_{1.2}Sb_{0.7}$, and $LaTeSb$. Details of the refinements are summarized in Table II. Lattice constants fit by least squares to indexed Guinier powder patterns matched those found for single crystals selected from these batches, as

shown in Table III. We have plotted our lattice constants as a function of Sb concentration in Fig. 1 for comparison to those of previous workers. Our data follow a similar trend of decreasing a and b parameters and increasing c parameter with increasing Sb content. However, for each stoichiometry, disagreement in the lattice constants is evident between the two studies. In the earlier report, nominal stoichiometries are given according to starting material concentrations, with no independent measurement of the Sb concentration. In our electron microprobe analysis, we found Sb levels consistently lower than such nominal compositions, and note that if the compounds reported by previous workers had a similar Sb deficiency, the trend would be to bring the data into closer agreement. A second deviation from earlier work is that we find a small difference between the a and b parameters for $LaTe_2$, previously reported as tetragonal.[32]

No direct evidence for superstructure was found in the x-ray studies of $LaTe_{2-x}Sb_x$ phases having $x<1$, due to the low intensities of the superlattice reflections. Preliminary Weissenberg and Precession camera experiments revealed no evidence for unit cells larger than the $LaTe_2$ type in any of the $LaTe_{2-x}Sb_x$ phases studied. Systematic absences for the subcell data sets were consistent with the space groups $Pm2_1n$, $P2_1mn$, and $Pmmn$. Since refinement in the acentric groups revealed no additional structural information, we report the substructures in the centric group $Pmmn$. For the phases $LaTe_{1.8}Sb_{0.2}$, $LaTe_{1.6}Sb_{0.3}$, and $LaTe_{1.2}Sb_{0.7}$, the subcell refinements indicate thermal ellipsoid anisotropy for atoms in the square-sheet layers, suggestive of displacements

TABLE V. The z fractional coordinate ($\times 10^4$) and displacement parameters ($\text{Å}^2 \times 10^3$) for $LaTe_{1.6}Sb_{0.3}$.

	z	U_{11}	U_{22}	U_{33}	U (eq)
La (1)	7252 (1)	11 (1)	12 (1)	14 (1)	12 (1)
Te (1)	3684 (1)	11 (1)	12 (1)	11 (1)	11 (1)
Sb/Te (2)	0	13 (1)	37 (1)	10 (1)	20 (1)
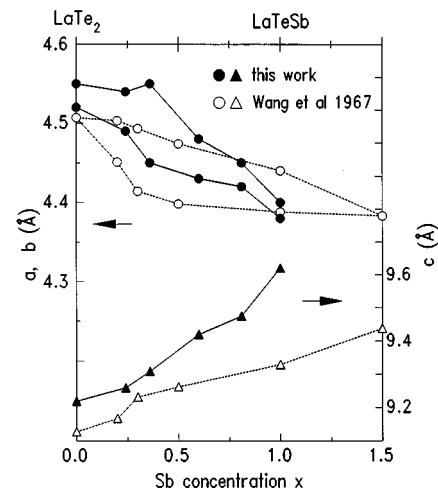
FIG. 1. Lattice parameters for the $LaTe_{2-x}Sb_x$ compounds. Circles: a and b, left axis; triangles: c, right axis. Solid symbols are from this report, open symbols are the data of Wang, Steinfink, and Kaman (Ref. 22).

TABLE VI. The z fractional coordinate ($\times 10^4$) and displacement parameters ($\text{Å}^2 \times 10^3$) for $LaTe_{1.2}Sb_{0.7}$.

	z	U_{11}	U_{22}	U_{33}	U (eq)
La (1)	7768 (1)	13 (1)	11 (1)	14 (1)	13 (1)
Te (1)	11287 (1)	13 (1)	11 (1)	14 (1)	13 (1)
Sb/Te (2)	5009 (1)	20 (1)	24 (1)	13 (1)	19 (1)

in the layer plane. Although reports on other structures in the RX_n family have shown occupational deficiencies for sites in the square-sheet layers,[33] we were not able to refine such features here as their parameters are highly correlated to the anomalous thermal parameters. Atomic coordinates and displacement parameters for these phases are summarized in Tables IV–VI.

By contrast, a commensurate superstructure was observed for LaTeSb. Long exposure rotation photos around the **c*** axis for LaTeSb showed a doubling of the **c** axis. For this phase the superlattice data were collected and refined on, yielding the supercell with $a_{super} = a_{sub}$, $b_{super} = b_{sub}$, and $c_{super} = 2c_{sub}$. Systematic absences were checked carefully due to the weakness of the superlattice reflections collected, and found to be most compatible with the space group $Pmcn$.[34] For all $LaTe_{2-x}Sb_x$ compounds we anticipate that substitution of Sb for Te should occur at the square-sheet sites, as the more electronegative Te is expected to prefer the more ionic site of the mixed La-Te layer. For LaTeSb all the square-sheet sites should thus be occupied by Sb atoms. However, the minute difference in Sb and Te scattering factors allows only minimal confirmation of this. In the LaTeSb refinement we find $R_1 = 3.46\%$ for Sb in the square sheets, and $R_1 = 3.55\%$ for Te in the sheet positions. The complete structure was found by direct methods and is of the CeAsS structure type.[35] In this structure, the square-sheet layer is distorted within the plane to form infinite zig-zag chains of Sb atoms along the **a** axis. The distortion reduces the nearest-neighbor Sb-Sb distance from 3.105 Å in the square lattice to 2.957 Å within the chains, while the distance between atoms on adjacent chains is 3.259 Å. La and Te atom positions are found to be modulated to a lesser degree. Atomic coordinates, displacement parameters, and selected interatomic distances and bond angles are presented in Tables VII–IX. The distortion of the primitive $\sqrt{a} \times \sqrt{a}$ square lattice takes place within the $a \times a$ LaTeSb unit cell, so that we can characterize the distortion in the Sb square sheets by the wave vector $\mathbf{q} = \mathbf{a}^*$. This interpretation will be addressed further below.

C. Transmission electron microscopy

Crystals from the $LaTe_{2-x}Sb_x$ phases were investigated through transmission electron microscopy. In order to search for superstructure reflections corresponding to the displacements of square-sheet atom positions, selected area electron-diffraction patterns were obtained parallel to the [001] zone axis. In this geometry, the beam is parallel to the layer stacking direction (**c** axis) and perpendicular to the flat platelet. Representative electron-diffraction patterns from each $LaTe_{2-x}Sb_x$ phase studied are shown in Fig. 2. In all of these patterns, intense main peaks corresponding to the $LaTe_2$-type subcell are observed. These $(hk0)$ reflections satisfy the con-

dition that $h+k$ is even, appropriate to the space group $Pmmn$ assigned from x-ray diffraction. Two groups of additional reflections are also observed. In Figs. 2(a) through 2(e), satellite reflections occur at wave vectors $\pm\mathbf{q}$ around reciprocal-lattice points, while in Fig. 2(f) weak reflections on reciprocal-lattice points with $h+k$ odd are present. We will address these two sets of extra reflections separately.

Reciprocal-lattice reflections $(hk0)$ with $h+k$ odd are forbidden for the LaTeSb structure, due to the relative orientations of the Sb sheet distortions in alternate Sb layers in the $a \times b \times 2c$ supercell. However, reflections having $h+k$ odd are weakly observed in our diffraction patterns for LaTeSb. Such forbidden reflections can be produced by a combination of sample bending and stacking disorder, as we found previously in our investigations of the RTe_3 system.[20] Reflections with $h+k$ odd are present in the Laue zones having $l \geq 1$ for the $LaTe_2$ structure. We investigated LaTeSb through converged beam electron diffraction and bright field imaging. We find that the reflections with $h+k$ odd belong to the higher-order Laue zone, and are projected onto the zero layer through a combination of stacking disorder and sample bending, exactly as reported previously for the RTe_3.[20]

Satellite reflections at wave vector $\pm\mathbf{q}$ around reciprocal-lattice points are observed for $LaTe_{2-x}Sb_x$ with $x < 1$, and indicate the presence of an additional periodicity of wavelength $2\pi/q$ superimposed on the square-sheet atom positions. Within each batch, diffraction patterns were obtained on several different crystals. Figure 3 shows the variation of q/a^* from crystal to crystal within each of the batches. For LaTeSb no superlattice reflections are visible through electron diffraction in the $(hk0)$ plane, as the extra reflections occur at multiples of $\mathbf{c}^*/2$. For this reason we include the superlattice wave vector $\mathbf{q} = \mathbf{a}^*$ determined from x-ray diffraction. The horizontal distribution of the symbols reflects the uncertainty in assigning an electron concentration from the microprobe measurements. The dashed line is a theoretical wave vector which will be addressed further below.

The experimental diffraction patterns can be reproduced by small periodic distortions in planar square Te sheets. For $LaTe_2$, the superlattice wave vector $\mathbf{q} = \mathbf{a}^*/2$ implies that a doubling of the unit cell in the **a** direction is present, as has been reported previously for the rare-earth diselenides.[18] The upper illustration in Fig. 4(a) illustrates the distorted square sheet in the 1×2 supercell of $LaSe_2$, having Se atom displacements of approximately $10\%a$. Simulated electron-diffraction patterns of Te square sheets having this large distortion yield intense satellite reflections comparable to the main peaks, an effect not observed experimentally for $LaTe_2$. Closer correspondence to the electron-diffraction pattern can be obtained by reducing the distortion amplitude by a factor of two, yielding the model Te sheet superstructure shown in the lower illustration in Fig. 4(a), which produces the simulated diffraction pattern shown in Fig. 4(b).

TABLE VII. Atomic coordinates ($\times 10^4$) for LaTeSb.

	x	y	z
La (1)	2500	2642 (1)	3610 (1)
Te (2)	2500	2628 (2)	1868 (1)
Sb (3)	−2500	2258 (2)	5009 (1)
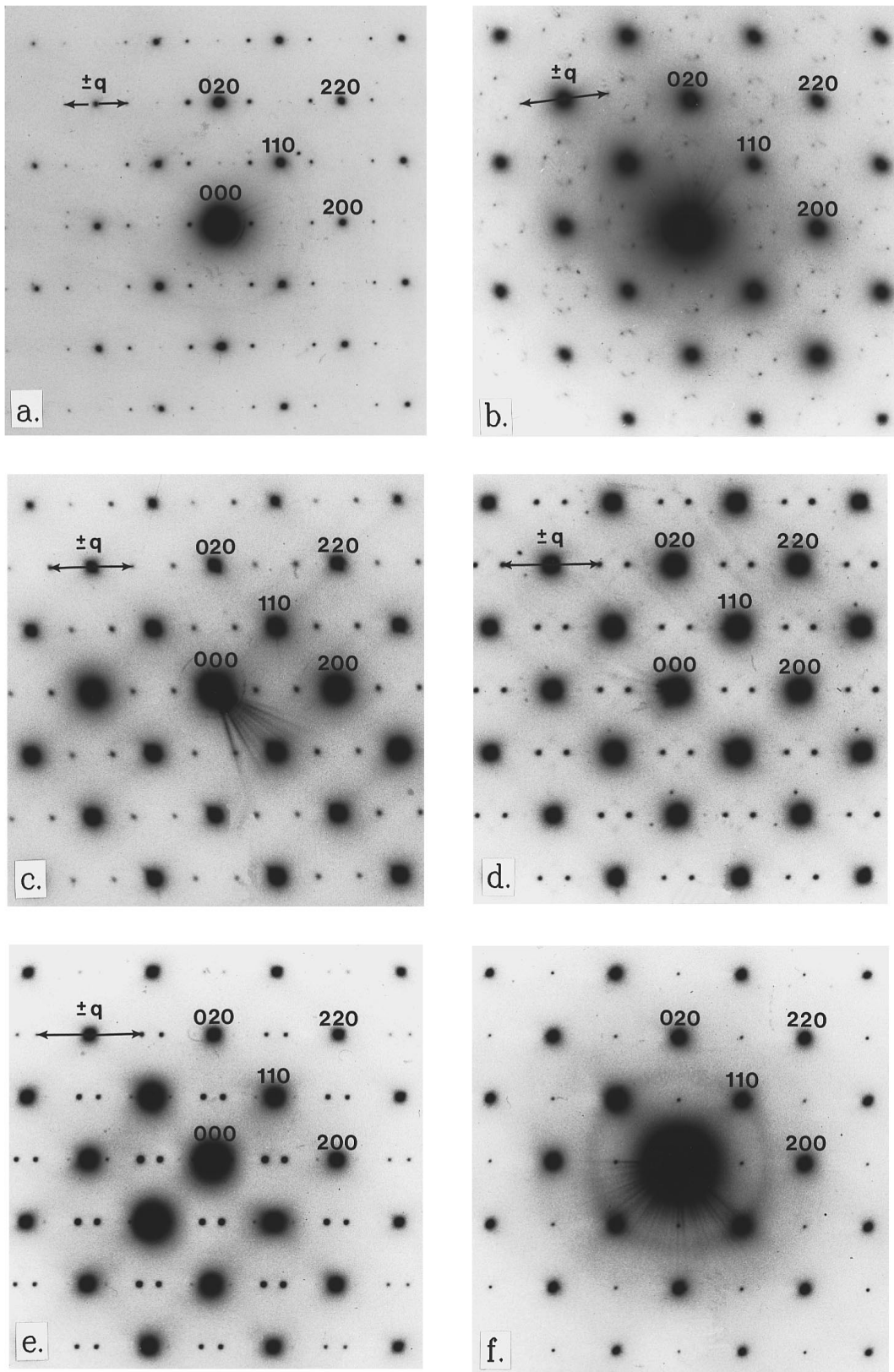
FIG. 2. Selected area diffraction patterns for $LaTe_{2-x}Sb_x$ samples aligned near the [001] axis. Strong ($hk0$) reflections with $h+k$ even correspond to the $LaTe_2$-type sublattice. (a) $LaTe_2$, with satellites $\mathbf{q} \approx (1/2)\mathbf{a}^*$. Very weak reflections on reciprocal-lattice points with $h+k$ odd may be produced by double diffraction, or the combination of stacking disorder and sample bending. (b) $LaTe_{1.8}Sb_{0.2}$, $\mathbf{q} = 0.672\mathbf{a}^* + 0.078\mathbf{b}^*$. (c) $LaTe_{1.6}Sb_{0.3}$, $\mathbf{q} \approx (\frac{2}{3})\mathbf{a}^*$. (d) $LaTe_{1.4}Sb_{0.5}$, $\mathbf{q} = 0.763\mathbf{a}^*$. (e) $LaTe_{1.2}Sb_{0.7}$, $\mathbf{q} = 0.836\mathbf{a}^*$. (f) LaTeSb. Forbidden reflections on reciprocal-lattice points with $h+k$ odd are produced by the combination of stacking disorder and sample bending, as described in the text.

TABLE VIII. Anisotropic and equivalent isotropic displacement parameters[a] ($\text{Å}^2 \times 10^3$) for LaTeSb.

	U_{11}	U_{22}	U_{33}	U_{23}	U (eq)
La (1)	8 (1)	11 (1)	10 (1)	0 (1)	10 (1)
Te (2)	9 (1)	11 (1)	11 (1)	0 (1)	10 (1)
Sb (3)	10 (1)	13 (1)	11 (1)	0 (1)	11 (1)

[a]The anisotropic displacement factor exponent takes the form: $-2\pi^2[h^2 a^{*2} U_{11} + \ldots + 2hka^*b^* U_{12}]$, with $U_{13} = U_{12} = 0$. U (eq) is defined as one-third of the trace of the orthogonalized U_{ij} tensor.

For the four LaTe$_{2-x}$Sb$_x$ phases having $0 < x < 1$, the observed diffraction patterns can be produced by square Te superlattices having small amplitude distortions in which the sheet atom displacements δx and δy in the **a** and **b** directions have the sinusoidal form

$$\delta x = A \sin(\mathbf{q} \cdot \mathbf{r}), \quad \delta y = A \cos(\mathbf{q} \cdot \mathbf{r}),$$

where the displacement amplitude $A \approx 0.03a$, **q** is the superlattice wave vector observed, and **r** denotes the undistorted atom positions. Figures 4(c) and 4(d) shows simulated diffraction patterns for square Te lattices with distortion wave vectors corresponding to those observed for LaTe$_{1.8}$Sb$_{0.2}$ and LaTe$_{1.6}$Sb$_{0.3}$. Similar simulations were obtained for LaTe$_{1.4}$Sb$_{0.5}$ and LaTe$_{1.2}$Sb$_{0.7}$. For these two compounds, the superlattice wave vector ($\mathbf{a}^* - \mathbf{q}$) was chosen for the model, with an $180°$ phase shift between rows of atoms, exactly as reported previously for the RTe$_3$ system.[20] The experimental LaTe$_{1.8}$Sb$_{0.2}$ diffraction pattern exhibits a twinning law that can be simulated by superimposing the pattern of Fig. 4(c) with the same pattern rotated $180°$ around the [110] axis. In the other phases, satellites were sometimes observed in both $\mathbf{a}^*$ and $\mathbf{b}^*$ directions, attributable to diffraction from layers having perpendicularly oriented distortions. In the case of LaTe$_{1.4}$Sb$_{0.5}$ perpendicular sets of satellites could be obtained by translating the sample, suggesting the presence of superlattice domains side by side in the crystal. Unfortunately, attempts to see these domains through dark field imaging in the two sets of satellites were unsuccessful due to the close spacing of the reflections relative to the size of the aperture available on the microscope.

TABLE IX. Selected interatomic distances (Å) and bond angles (degrees) for LaTeSb.

La (1)-Te (2)	3.2340	(7)
La (1)-Te (2)	3.2422	(7)
La (1)-Te (2)	3.3509	(10)
La (1)-Sb (3)	3.4227	(11)
La (1)-Sb (3)	3.4741	(9)
La (1)-Sb (3)	3.4787	(10)
Sb (3)-Sb (3)	2.9574	(10)
Sb (3)-Sb (3)	3.2592	(11)
Sb (3)-Sb (3)-Sb (3)	95.48	(4)
Sb (3)-Sb (3)-Sb (3)	84.38	(4)
Sb (3)-Sb (3)-Sb (3)	174.29	(4)
Sb (3)-Sb (3)-Sb (3)	90.055	(11)

While our observations for these compounds are consistent with small sinusoidal displacements, we cannot rule out the possibility that more complicated superstructures are present. For LaTe$_{1.6}$Sb$_{0.3}$, the first-order satellites occur at the wave vectors $(\frac{1}{3})\mathbf{a}^*$ and $(\frac{2}{3})\mathbf{a}^*$. Higher-order satellites, indicating deviation from the sinusoidal distortion in the 1×3 supercell, would also fall on multiples of $(\frac{1}{3})\mathbf{a}^*$, so their presence cannot be ruled out. In the other phases, faint satellite reflections are sometimes observed at the wave vector $\pm 2\mathbf{q}$, and although it is possible that they are second-order satellites, they may also be produced by double diffraction. Further single-crystal x-ray studies will be necessary to determine the details of these superstructures.

IV. DISCUSSION

We have attributed the superlattice peaks in LaTe$_{2-x}$Sb$_x$ for $x \le 1$ to periodic distortions in the square-sheet atom positions. The observed superlattice wave vectors are close to those which nest large parallel sheets of the Fermi surfaces calculated for square Te sheets. Figure 5 shows the evolution of Fermi surfaces calculated for two-dimensional square Te sheets as the band filling is continuously varied between 7.0 e/sheet atom in LaTe$_2$ and 6.0 e/at. in LaTeSb. The extended-Hückel method[36] with conventional Te parameters was employed,[37] using the single atom primitive square cell with lattice constant $a/\sqrt{2}$.[38] Calculations performed for square Sb sheets at similar band fillings give nearly identical results.[39] Band filling was determined using a model incorporating charge transfer from trivalent La to Te or Sb atoms in completely ionic La-anion layers and fully occupied square sheets. For LaTe$_2$ these assumptions require that each La atom contributes two electrons to the Te atom in the R-Te layer, and one to the square-sheet Te atom, yielding seven electrons per Te in the square-sheet bands. For LaTe$_{2-x}$Sb$_x$, the electron count in the sheets is modified to $(7-x)$ electrons per sheet anion, as Sb has one fewer valence electron than Te. The Fermi surface has a first Brillouin zone of width $\sqrt{2}(2\pi/a) \equiv \sqrt{2}a^*$. Solid and dashed lines in Fig. 5 distinguish the two bands that cross the Fermi level. For both the lower (dashed) band near Γ and the upper (solid) band crossing the Fermi level near M, the filled states lie towards M in the Brillouin zone.

Comparison of the experimental superlattice wave vectors to the calculated Fermi surfaces shows that distortions occur at geometrically plausible nesting vectors for the entire doping range. The superlattice wave vectors observed through the diffraction measurements are shown as arrows on the figure. For LaTe$_2$ [Fig. 5(a)], a doubling of the unit cell in the $\mathbf{a}^*$ direction connects small sections of the Fermi surface of the upper band. With the slight difference in band filling realized in LaTe$_{1.8}$Sb$_{0.2}$, the upper bands are nested by a slightly larger wave vector, and the observed superlattice wave vector $\mathbf{q} = 0.672\mathbf{a}^* + 0.078\mathbf{b}^*$ has become incommensurate to accommodate the change in nesting [Fig. 5(b)]. In LaTe$_{1.6}$Sb$_{0.3}$ our results suggest that it is equally favorable to nest states across the two separate sheets which comprise the Fermi surface [Fig. 5(c)]. As more electrons are removed from the system, these nesting sheets are gapped by a progressively larger wave vector, as observed experimentally for LaTe$_{1.4}$Sb$_{0.5}$ [Fig. 5(d)] and LaTe$_{1.2}$Sb$_{0.7}$ [Fig. 5(e)]. For
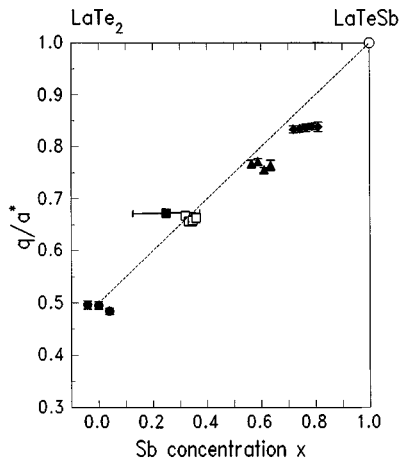
FIG. 3. Magnitude of q/a^* as a function of Sb concentration, for all TEM samples investigated. The horizontal distribution of the symbols reflects the uncertainty in Sb concentration, indicated as a horizontal error bar for $LaTe_{1.8}Sb_{0.2}$. ●: $LaTe_2$; ■: $LaTe_{1.8}Sb_{0.2}$; □: $LaTe_{1.6}Sb_{0.3}$; ▲: $LaTe_{1.4}Sb_{0.5}$; ◆: $LaTe_{1.2}Sb_{0.7}$; ○: LaTeSb, determined from x-ray diffraction. Dashed line: theoretical Fermi-surface nesting vector as described in text.

LaTeSb [Fig. 5(f)], the commensurate superlattice wave vector of $\mathbf{q}=\mathbf{a}^*$ is observed. As Fig. 5(f) shows, the distortion wave vector $\mathbf{q}=\mathbf{a}^*$ yields perfect nesting for the calculated Fermi surface with 6.0 e/sheet anion. Here, no Te remains in the square sheet and the Sb atoms distort from the square lattice to form infinite chains in the layer plane. Distorted As and P square nets having similar twofold coordination are found in the RAsS and RPS systems, which are isoelectronic with LaTeSb and share the same substructure.[40,41] In earlier reports the reduction in As or P coordination in the square sheets has been interpreted in terms of the formation of covalent bonds. Although this interpretation would be adequate for LaTeSb considered alone, in the context of the $LaTe_{2-x}Sb_x$ series the LaTeSb superstructure is more generally regarded as a Fermi-surface nesting CDW. The correspondence between the geometry of the calculated Fermi surfaces and the observed superlattice wave vectors argues that the distortions in the $LaTe_{2-x}Sb_x$ system are due to charge-density waves driven by the considerable nesting of the very simple square-sheet band structure.

While it is plausible that the observed distortion wave vectors optimally nest the calculated Fermi surfaces, we have not demonstrated that CDW's at these wave vectors are the most energetically favorable. For example, a combination of vertical and horizontal nesting vectors would also nest large sections of the Fermi surfaces, particularly at low electron concentrations, and may, in principle, produce a greater reduction in the energy of the electronic states. Analysis of this problem requires that we consider both the geometry and the dispersion of the bands at the Fermi surface, both of which determine the electronic energy gain of the CDW. Such a treatment must include the contributions not only of the flat surfaces but also the corners of the Fermi-surface sheets, whose sensitivity to the model parameters may well compromise the analysis.

However, we can gain some insight into the system's preference for distortions parallel to $\mathbf{a}^*$, by considering the
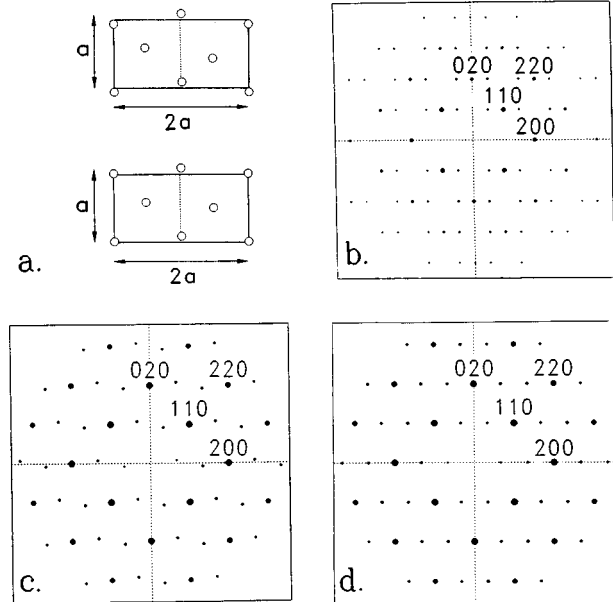
FIG. 4. (a) Top: Distorted Se sheet of $LaSe_2$. Circles show the atom positions in the $a \times 2a$ supercell (solid lines), while the dashed line shows the boundary of the $a \times a$ $LaSe_2$ subcell. Bottom: Model Te sheet supercell with $LaSe_2$ distortion pattern of smaller amplitude. (b) Simulated selected area diffraction pattern of the Te sheet model in (a), showing satellite reflections at $\mathbf{q}=\pm\mathbf{a}^*/2$ as observed for $LaTe_2$. (e) Simulated diffraction pattern of $LaTe_{1.8}Sb_{0.2}$, with a sinusoidal distortion in a 3×13 supercell, with wave vector $q_x/a^*=3/2$, $q_y/a^*=\frac{1}{13}$. (d) $LaTe_{1.6}Sb_{0.3}$, 1×3 supercell, $q/a^*=\frac{2}{3}$.

Fermi surface derived from nearest-neighbor bonding of chalcogen p orbitals. Figure 6(a) illustrates the p_x and p_y orbitals of chalcogen atoms in a square lattice. We assume that the p_x orbitals interact only with their nearest neighbors in the x direction. Bands derived from these orbitals will have no dispersion in the k_y direction, and the constant energy surfaces will be planes normal to k_x. If the p_y orbitals of the Te atoms are taken to interact independently, the Fermi surface will consist of two perpendicular pairs of lines, as shown in Fig. 6(b) for the band fillings of $LaTe_2$ (7.0 e/sheet atom, solid lines) and LaTeSb (6.0 e/at., dashed lines). Here perfect Fermi-surface nesting is achieved by the diagonal wave vector joining the points where the perpendicular surfaces intersect, a conclusion which is not dependent on model parameters. The theoretical nesting vector for this model, shown as a function of electron concentration in Fig. 3, agrees remarkably well with the experimentally observed CDW wave vectors for $LaTe_{2-x}Sb_x$ compounds. For $LaTe_2$, this model predicts the commensurate nesting vector better than the extended-Hückel calculation, which shows only marginal nesting for $\mathbf{q}=\mathbf{a}^*/2$. The Fermi surfaces determined from the extended-Hückel calculations are similar to those derived from nearest-neighbor interactions, as shown by the dashed line in Fig. 6(c) for the intermediate filling of 6.6 e/at. The curvature of the Fermi-surface sheets which is evident in the extended-Hückel calculations is a consequence of interactions between further neighbors, controlled by the choice of an overlap parameter. Although these second-order effects change the Fermi-surface geometry, the nearest-
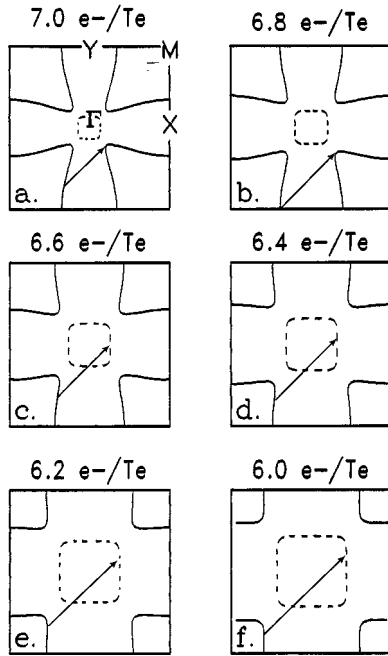
FIG. 5. Fermi surfaces calculated for square Te sheets having band fillings appropriate to the $LaTe_{2-x}Sb_x$ samples studied. Solid and dashed lines distinguish the two bands that cross the Fermi level. Arrows on each figure indicate the superlattice wave vector observed through TEM for each stoichiometry. (a) $LaTe_2$. (b) $LaTe_{1.8}Sb_{0.2}$. (c) $LaTe_{1.6}Sb_{0.3}$. (d) $LaTe_{1.4}Sb_{0.5}$. (e) $LaTe_{1.2}Sb_{0.7}$. (f) LaTeSb.

FIG. 6. (a) Model Te square lattice in which the only interactions considered are between neighboring orbitals pointing towards each other. The interaction between p_x orbitals depends only on their separation along the x direction, while the independent p_y orbitals interact along y. (b) Dashed lines: Simple model Fermi surface of Te sheet with 6.0 e/Te (LaTeSb) as described in text. Solid lines: Fermi surface for 7.0 e/Te ($LaTe_2$). The Fermi surfaces are perfectly nested by diagonal wave vectors, shown by an arrow for $LaTe_2$. (c) Dashed lines: Simple model Fermi surface for Te sheet with 6.6 e/Te. Solid lines: extended-Hückel calculation for the same band filling.

neighbor interactions are apparently predominant in determining the optimal Fermi-surface nesting.

V. SUMMARY

We have grown single crystals of six members of the series $LaTe_{2-x}Sb_x$ with $0 \le x \le 1$ using an alkali halide flux method, determining the stoichiometry through electron microprobe analysis. Powder and single-crystal x-ray measurements elaborate upon the layered structures reported previously for these phases, in which planar square lattices alternate with rare-earth anion layers, with Sb substituting for Te within the $LaTe_2$ structure type. Through electron diffraction we find satellite reflections indicating the presence of small amplitude distortions in the layer plane of the square sheets for phases with $x<1$. These periodic distortions occur at wave vectors which span large parallel sheets of the Fermi surfaces determined from extended-Hückel calculations on square Te lattices. Single-crystal x-ray refinements indicate that LaTeSb has the CeAsS-type structure, with a distortion in the Sb square lattice at a wave vector which perfectly nests the calculated Fermi surface. The CDW distortions are stable at room temperature over the range of band filling obtained from $LaTe_2$ to LaTeSb. We find no evidence that disordered occupation of Te sites by Sb affects CDW stability. Our work demonstrates that the $LaTe_{2-x}Sb_x$ host Fermi-surface driven CDW's, in which the band filling and the CDW wave vector can be continuously tuned, and which can be understood from a very simple model involving planar Te square lattices.

*Present address: Physics Department, Brookhaven National Laboratory, Upton, NY 11973-5000.

†Author to whom correspondence should be addressed.

[1] F. J. DiSalvo, in *Electron-Phonon Interactions and Phase Transitions*, edited by T. Riste (Plenum, New York, 1977).

[2] R. H. Friend and D. Jérome, J. Phys. C **12**, 1441 (1979).

[3] *Electronic Properties of Inorganic Quasi-One-Dimensional Compounds*, edited by P. Monceau (Reidel, Dordrecht, 1985).

[4] *Crystal Chemistry and Properties of Materials with Quasi-One-Dimensional Structures*, edited by J. Rouxel (Reidel, Dordrecht, 1986).

[5] D. E. Cox and A. W. Sleight, Solid State Commun. **19**, 969 (1976).

[6] S. Uchida, S. Tajima, A. Masaki, S. Sugai, K. Kitazawa, and S. Tanaka, J. Phys. Soc. Jpn. **54**, 4395 (1985).

[7] L. F. Mattheiss and D. R. Hamann, Phys. Rev. B **28**, 4227 (1983).

[8] A. W. Sleight, J. L. Gillson, and P. E. Bierstedt, Solid State Commun. **17**, 27 (1975); D. E. Cox and A. W. Sleight, in *Proceedings of the Conference on Neutron Scattering, Gatlinburg, Tennessee*, edited by R. M. Moon (National Technical Information Service, Springfield, VA, 1976).

[9] L. F. Mattheiss, E. M. Gyory, and D. W. Johnson, Jr., Phys.

Rev. B **37**, 3745 (1988), and references therein.

[10] R. J. Cava *et al.*, Nature (London) **332**, 814 (1988).

[11] S. Tajima, S. Uchida, A. Masaki, H. Takagi, K. Kitazawa, and S. Tanaka, Phys. Rev. B **32**, 6302 (1985).

[12] J. A. Wilson, F. J. DiSalvo, and S. Mahajan, Adv. Phys. **24**, 117 (1975).

[13] D. E. Moncton, J. D. Axe, and F. J. DiSalvo, Phys. Rev. B **16**, 801 (1977).

[14] M.-H. Whangbo and E. Canadell, J. Am. Chem. Soc. **114**, 9587 (1992).

[15] R. Wang, H. Steinfink, and W. F. Bradley, Inorg. Chem. **5**, 142 (1966).

[16] B. K. Norling and H. Steinfink, Inorg. Chem. **5**, 1488 (1966).

[17] M.-P. Pardo and J. Flahaut, Bull. Soc. Chim. **10**, 3658 (1967).

[18] J.-P. Marcon and R. Pascard, C. R. Acad. Sci. Paris **266**, 270 (1968); S. Bénazeth, D. Carré, and P. Laruelle, Acta Crystallogr. Sec. B **38**, 33 (1982).

[19] B. Foran, S. Lee, and M. C. Aronson, Chem. Mater. **5**, 974 (1993); S. Lee and B. Foran, J. Am. Chem. Soc. (to be published).

[20] E. DiMasi, M. C. Aronson, J. F. Mansfield, B. Foran, and S. Lee, Phys. Rev. B **52**, 14 516 (1995).

[21] X. Zhang *et al.*, J. Am. Chem. Soc. **117**, 10 513 (1995).

[22] R. Wang, H. Steinfink, and A. Raman, Inorg. Chem. **6**, 1298 (1967).

[23] K. S. V. L. Narasimhan and H. Steinfink, Mater. Sci. Eng. **3**, 309 (1968/69).

[24] The RbCl/LiCl eutectic ratio of 45 at. % RbCl was used, with typically 0.5 g of flux and 0.1–0.2 g La in each batch. $LaTe_2$ was obtained from a tube containing elemental Ca, with a nominal Ca:La ratio of 2 at. %, in an attempt to substitute Ca for La. Electron microprobe analysis of the $LaTe_2$ crystals found less than 0.001 wt % Ca, while atomic absorption spectroscopy found less than 0.1 wt % Ca, statistically insignificant amounts.

[25] Cameca MBX automated microprobe WDS system with Te, Sb, and $LaPO_4$ standards. Standardization of La was checked by measurements on freshly cleaved $LaTe_3$ crystals.

[26] Cu $K\alpha_1$; $\lambda = 1.5404$ Å, with NBS (NIST) powdered silicon used as an internal reference standard.

[27] LAZY-PULVERIX: K. Yvon, W. Jeitschko, and E. J. Parthé, J. Appl. Cryst. **10**, 73 (1977).

[28] Siemens P4 Diffractometer, Mo $K\alpha$; $\lambda = 0.71073$ Å, data were recorded full sphere for each crystal over a θ range of 4.3–32.5°, by $\theta - 2\theta$ scans, at room temperature. No crystal decay was observed in the intensities of three check reflections measured every 100 data points. Azimuthal scans were recorded for semiempirical absorption corrections. Data were Lorentz and polarization corrected. All atoms were found by direct methods, and refined by full-matrix least squares on F^2.

[29] See AIP Document No: PAPS PRBMD0-54-xxxx-20 for 20 pages of powder data and single crystal-structure determination. Order by PAPS number and journal reference from American Institute of Physics, Physics, Physics Auxiliary Publication Service, Carolyn Gehlbach, 500 Sunnyside Bouldevard, Woodbury, NY 11797-2999. Fax: 516-576-2223, e-mail: paps@aip.org. The price is $1.50 for each microfiche (98 pages) or $5.00 for photocopies of up to 30 pages, and $0.15 for each additional page over 30 pages. Airmail additional. Make checks payable to the American Institute of Physics.

[30] CERIUS^2 Chemical Simulations Software Package, Molecular Simulation Inc., Burlington, MA, 1994.

[31] M.-H. Whangbo, R. Hoffmann, and R. B. Woodward, Proc. R. Soc. London Ser. A **366**, 23 (1979).

[32] R. Wang, H. Steinfink, and W. F. Bradley, Inorg. Chem. **5**, 142 (1966).

[33] P. Plambeck-Fischer, W. Abriel, and W. Urland, J. Solid State Chem. **78**, 164 (1989).

[34] We have chosen this nonconventional setting because it leaves the structure oriented for comparison with the other structures reported here; the conventional space group *Pnma* (No. 62) is obtained by the application of the transformation matrix (0 1 0, 1 0 0, 0 0 1).

[35] R. Ceolin, N. Rodier, and P. Khodadad, J. Less-Common Met. **53**, 137 (1977).

[36] R. Hoffmann, J. Chem. Phys. **39**, 1397 (1963); M.-H. Whangbo, R. Hoffmann, and R. B. Woodward, Proc. R. Soc. London Ser. A **366**, 23 (1979).

[37] We used 170 k points per octant of the Brillouin zone, with Te parameters from E. Canadell, Y. Mathey, and M.-H. Whangbo, J. Am. Chem. Soc. **110**, 104 (1988).

[38] Previously we have reported Fermi surfaces calculated for the centered two-atom chalcogen square cell, corresponding to the RX_n subcell with parameter a. Here we find it preferable to present calculations based on the primitive one-atom cell with spacing $a/\sqrt{2}$. We will continue to use a and $a^* \equiv 2\pi/a$ referenced to the two-atom cell, to facilitate comparison to the diffraction patterns indexed according to the RX_2 substructure.

[39] Sb parameters were from T. Hughbanks, R. Hoffmann, M.-H. Whangbo, K. R. Stewart, O. Eisenstein, and E. Canadell, J. Am. Chem. Soc. **104**, 3876 (1982).

[40] F. Hulliger, R. Schmelczer, and D. Schwarzenbach, J. Solid State Chem. **21**, 371 (1977).

[41] W. Tremel and R. Hoffmann, J. Am. Chem. Soc. **109**, 124 (1987).